

# GRID REFINEMENT USING SPECTRAL ERROR INDICATORS WITH APPLICATION TO AIRFOIL DNS

Markus Zauner<sup>1</sup>, Christian T. Jacobs<sup>2</sup> and Neil D. Sandham<sup>3</sup>

<sup>1</sup> University of Southampton  
University Road, SO17 1BJ  
m.zauner@soton.ac.uk

<sup>2</sup> University of Southampton  
University Road, SO17 1BJ  
christian@christianjacobs.uk

<sup>3</sup> University of Southampton  
University Road, SO17 1BJ  
n.sandham@soton.ac.uk

**Key words:** Structured grids, error indicator, direct numerical simulation, airfoil

**Abstract.** High-order direct numerical simulations of transitional and turbulent fluid flows require smooth grids with continuous metric terms across block boundaries. In this contribution we present an approach to generate and evaluate structured grids around airfoils with a blunt trailing edge that are continuous up to the second order of derivatives. Dassault Aviation's V2C airfoil is used as a case study, involving 3D as well as 2D simulations that solve the Navier-Stokes equations directly. The reference grid consists of more than one billion points to resolve the transonic flow at a Mach number and Reynolds number of  $M = 0.7$  and  $Re = 500,000$ , respectively. A spectral error indicator uses the Fourier spectrum of cube-shaped subdomains to identify critical regions of the grid, where refinement is needed. If the spectral energy of small-scale fluctuations in the flowfield does not decay faster than a certain minimum rate, it is assumed to be caused by the under-resolution of flow features. This methodology leads to a reduction in computational effort when designing and validating large complex grids. The contribution concludes by describing a best-practice procedure for the full grid generation process, including the refinement strategy.

## 1 INTRODUCTION

Direct numerical simulations (DNS), involving the application of high-order central difference methods for structured curvilinear multi-block grids, require continuous metric terms even across block boundaries. Otherwise, artificial disturbances are introduced in the right-hand side of the Navier-Stokes equations. Commercial software packages often apply methods that solve elliptic partial differential equations to increase the smoothness

of the grid. Those approaches are problematic for geometries with a blunt trailing edge within a three-block CH-grid configuration, as sketched in figure 1, and the computational effort increases significantly with larger grids. Furthermore, in a direct numerical simulation at higher Reynolds numbers, the grid has to cover a wide range of length scales. On the one hand, sufficient resolution of boundary- and shear-layers is required, whereas on the other hand a significantly lower resolution of the potential flow is desirable to keep the computational effort as low as possible. Without manual intervention, grid smoothing algorithms tend to shift points from the highly resolved regions into the freestream region. With respect to post-processing requirements, such as sound field and global stability analysis, it is also beneficial to control the spacing in the freestream region, avoiding large grid-spacing at the front part of the C-block in the tangential direction. As a consequence, it is necessary to apply s-shaped gridlines, which enable independent spacing at the wall surface and at the domain boundaries.

In the current contribution, we generate high-fidelity CH-type grids for airfoils with a blunt trailing edge. Emphasis is placed on the scalability of the grid generation process with respect to higher orders of continuity as well as larger grids for peta- and exa-scale simulations. The approach has been successfully tested and applied to DNS at moderate Reynolds numbers, using grids that consist of more than one billion points in the  $xy$ -plane, corresponding to figure 1.

In order to avoid extensive grid studies involving expensive 3D simulations, a recently developed error-severity indication tool (Jacobs et al., 2018) is applied to quantify the quality of grids a posteriori. This approach correlates derivative quantities such as vorticity to grid-to-grid point oscillations. We highlight the potential of this tool even at early stages in the grid-generation process. In the long term, such error-indicator tools aim to fully replace 3D grid studies.

## 2 Methodology

### 2.1 Grid generation

The computational domain is divided into three blocks consisting of one C-block ( $B2$ ) around the airfoil geometry and two H-type blocks ( $B1$  &  $B3$ ) enclosing the blunt trailing edge, wake region and outflow. Figure 1 shows (A) the arrangement of all three blocks and (B) the reference grid (denoted  $Nc$ ). The coordinates of the Cartesian coordinate system are denoted by  $x$  and  $y$ , whereas curvilinear coordinates are denoted by  $\xi$  and  $\eta$ . In order to increase the flexibility regarding the distribution of grid points, the airfoil surface is divided into four sections, labelled as  $C1$ ,  $C2$ ,  $C3$  and  $C4$ . The centre of rotation to adjust the angle of attack ( $\alpha$ ) is located at the half chord position  $[0.5c, 0]$ , where  $c$  denotes the axial chord length. For each section, the grid points as a function of distance along the surface are defined by a 6<sup>th</sup>-order polynomial that ensures a continuous transition between neighbouring sections. The coordinates are computed for each grid point on the surface, using a cubic spline interpolation method. The polynomials are defined by the number of points, surface distance, first and second derivatives on both sides (corresponding to neighbouring sections) and the third derivative at one side, which serves

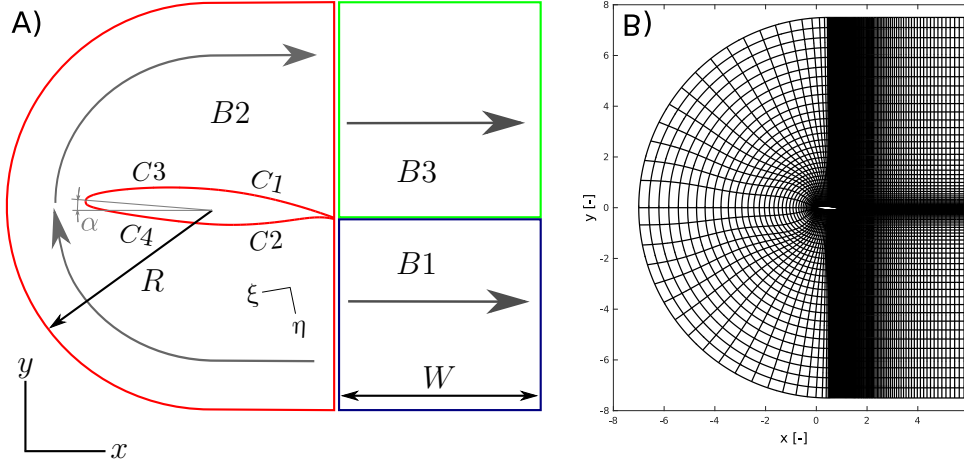


**Figure 1:** (A) Sketch of the three-blocks CH-grid topology, the segmentation of the airfoil surface (sections  $C1 - C4$ ) and (B) the reference grid (approximately every  $20^{th}$  point plotted).

as a control parameter for fine tuning. All derivatives are calculated by a fourth-order central difference scheme and the boundaries are treated with the method by Carpenter et al. (1999). In order to avoid intersections, gridlines cannot be wall-normal at every position along the airfoil. Therefore the wall angles of  $\eta$ -gridlines ( $\xi = const.$ ) need to be defined by a  $5^{th}$ -order polynomial as well. The same procedure is performed for the outer domain boundaries.

The shape of the  $\xi$ -gridlines ( $\eta = const.$ ) containing both corners of the blunt trailing edge in  $B1$  and  $B3$  is also determined by polynomial functions. Those gridlines are designed as continuous extensions of the upper and lower airfoil surface. Within a distance of  $1.5c$  from the trailing edge, the curvilinear  $\eta$ - and  $\xi$ -gridlines in the wake region transition to vertical and horizontal gridlines, respectively.

The  $\eta$ -gridlines in  $B2$  are generated by looping through each point on the airfoil surface in the clock-wise direction. The shape of each  $\eta$ -gridline is defined by three steps that are illustrated in figure 2. The aim is to find a smooth, contained transition from a wall-optimised curve (green curve in figure 2(A)) to a boundary-optimised curve (green curve in figure 2(B)), maintaining a homogeneous distribution of grid points in the farfield. In order to get the wall-optimised curve in figure 2(A), a blending procedure between the blue line, corresponding to defined gridline angles at the wall, and a red line, connecting the point at the wall (I) with the corresponding point at the boundary (II) is applied. In figure 2(B), the boundary-optimised curve is calculated in the same way considering a blue line associated to the pre-defined angle at the outer boundary. In order to generate the final  $\eta$ -gridline (magenta curve) for that specific point on the airfoil surface, both green curves are blended again according to figure 2(C). The spacings of points along each gridline is again defined by a  $6^{th}$ -order polynomial.

After finishing  $B2$ , gridlines for  $B1$  and  $B3$  are generated. Firstly, the  $\eta$ -gridlines between the  $\xi$ -gridlines passing through the corners and the outer boundaries are calculated in the same way as described for  $B2$ . Secondly, a blending is performed between two

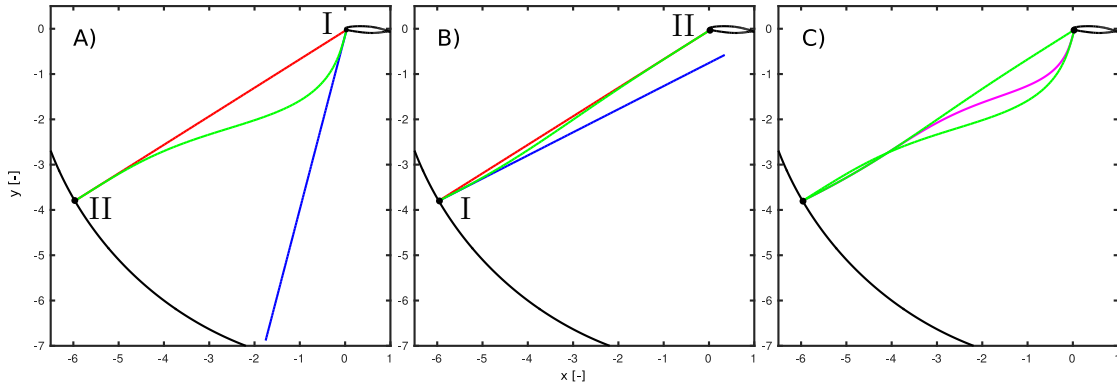


**Figure 2:** Illustration of the three steps to generate the  $\eta$ -gridlines in block 2.

straight lines corresponding to the angles that are defined a-priori for each point along the  $\xi$ -gridlines going through the corners of the blunt trailing edge. For this connection segment in the wake, constant spacing is applied, corresponding to the first cells of adjacent  $\eta$ -gridlines. Eventually, all three segments are merged and split into two parts according to  $B1$  and  $B3$ . The only discontinuities within the domain are the singular points at the corners of the trailing edge.

More details on the complete grid-generation process are presented by Zauner and Sandham (2018).

## 2.2 Error indicator

The error indicator used in this work is based on a spectral approach, in which the domain is partitioned into several cube-shaped subdomains, each comprising  $N_e^3$  grid points. A Fourier analysis is conducted within each subdomain to characterise the severity of any solution error caused by insufficient grid resolution in that region. The fundamental principle behind the indicator is that, if small-scale turbulent structures are well-resolved by the numerical grid, then their Fourier spectral energy is expected to decrease at a certain minimum acceptable rate. If this rate is not attained, then the grid is considered to not be fine enough and grid-to-grid point oscillations may appear. The general algorithm can be summarised in three steps as follows. For each error block, each of the  $N_e^2$  lines of points is considered in turn. For each line, step 1 is to apply a Hamming window to the field of interest in order to prepare the block for Fourier analysis. Step 2 is to compute 1D-Fourier amplitudes for  $k = N_e/2, N_e/4, N_e/8$ , with summations to avoid Fourier transforms; this is faster when considering only these 3 specific wavenumbers. Step 2 is then repeated for the other directions, which provides a degree of anisotropy. Step 3 is to take maximum values of each amplitude over all  $N_e^2$  lines, and use this to determine whether amplitudes are decreasing at rate greater than or equal to  $r$ . The severity of solution error is quantified by an integer-based measure (denoted  $I_i$ ), which takes into account the maximum Fourier amplitudes calculated in Step 3. The integer values are between 0 and 3 inclusive, where 0 indicates little/no error present and 3 indicates the worst possible error. A more detailed description and evaluation of the error indicator is

described by Jacobs et al. (2018). In the figures that follow, the severity values 0, 1, 2 and 3 are represented by green, blue, orange and red data points respectively. Furthermore, by applying the Fourier transform in each direction, the error indicator is able to suggest the direction that is most likely to exhibit grid-to-grid point oscillations and hence guide the necessary grid refinement.

### 2.3 Simulation

Three different grids representing Dassault Aviation’s V2C profile are tested by carrying out direct numerical simulations with a Mach number of  $M = 0.7$  and a Reynolds number of  $Re = 500,000$  at an angle of attack of  $\alpha = 4^\circ$ . The in-house code SBLI (Yao et al., 2009) is used to solve the transonic flow around the airfoil. For the spatial discretisation, a fourth-order central-difference scheme is applied, treating the boundaries according to Carpenter et al. (1999). The temporal discretisation involves a third-order low-storage Runge-Kutta scheme. Zonal characteristic boundary conditions (Sandberg and Sandham, 2006) are applied at the outflow, whereas integrated characteristic boundary conditions (Sandhu and Sandham, 1994) are enforced at all other outer boundaries in order to minimise reflections of acoustic waves. Periodic boundary conditions are applied in the spanwise direction. A total variation diminishing method with an additional switch is applied to increase the numerical stability around shock waves. Finally an implicit 6<sup>th</sup>-order filter is employed in the farfield and upstream of the leading edge to avoid numerical fluctuations in the freestream. Table 1 outlines the test cases that are discussed in the scope of this contribution. The reference simulation (case  $Nc_{3D}$ ) was run for 25

Case	$R/c$	$W/c$	$L_z/c$	$N_{\xi,2}$	$N_{\eta,2}$	$N_{\xi,1/3}$	$N_{\eta,1/3}$	$N_z$	$N_{total}$
$Nc_{3D}^*$	7.5	6.0	0.05	3045	999	1999	1023	150	$1.07 \cdot 10^9$
$Nc_{s,3D}$	7.5	6.0	0.05	3045	999	1999	1023	250	$1.78 \cdot 10^9$
$Od_{3D}$	7.5	6.0	0.05	4570	1299	1999	1323	150	$1.68 \cdot 10^9$
$Nc_{2D}$	7.5	6.0	—	3045	999	1999	1023	1	$7.13 \cdot 10^6$

\* reference simulation with reference grid  $Nc$

**Table 1:** Numerical grid details considering different levels of resolution.  $R$  and  $W$  denote the radius of the C-block and the length of block 1, respectively.  $L_z$  indicates the spanwise domain width.  $N_{\xi,2}$  and  $N_{\eta,2}$  are the number of grid points of  $B2$  around the aerofoil in the  $\xi$  and  $\eta$  direction, respectively, whereas  $N_{\xi,1/3}$  and  $N_{\eta,1/3}$  denote the number of grid points in  $B1$  and  $B3$  to resolve the wake.  $N_z$  denotes the spanwise resolution and  $N_{total}$  expresses the total number of grid points.

time units ( $t = c/U_\infty$ ). Figure 3(A) shows an instantaneous 2D-snapshot of the  $x$ -velocity component  $U$ , a supersonic region over the suction-side airfoil surface and a self-sustaining transition to turbulence on both sides. Upstream-propagating shock waves are indicated by the unsteady sonic line (black curve). Kelvin-Helmholtz (KH) vortex structures in the shear layers are observed on both sides as well. Zauner et al. (2018) describes the simulation and the observed flow phenomena in more detail.

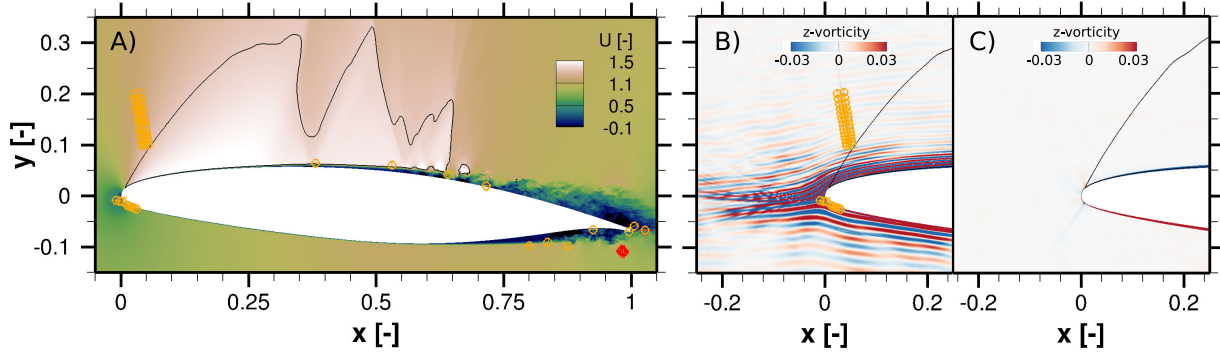


**Figure 3:** Instantaneous snapshots of case  $Nc_{3D}$  showing (A)  $x$ -component of velocity and (B)  $z$ -vorticity contours at  $t = 3.7$ . (C) Snapshot of  $z$ -vorticity contours at  $t = 11.8$ . Error-severity levels 2 and 3 are displayed by orange and red circles, respectively. The black curves denote the sonic line ( $M = 1$ ).

### 3 Error indicator analysis

#### 3.1 Analysis of reference case

The spectral error-indicator is applied to the instantaneous vorticity flowfield at a simulation time of  $t = 3.7$  before employing the 6<sup>th</sup>-order filter and highlights critical regions with an error-severity level of  $I_i = 3$  by red circles in figure 3(A), whereas less critical regions ( $I_i = 2$ ) are marked by orange circles. Severity levels of  $I_i < 2$  are neglected in this plot. A region outside the shear layer on the pressure side shows critical error-severity levels in the  $\eta$ -direction, which seem to be caused by a strong vortex propagating into a slightly coarser grid region. Closer to the shear layers on both sides, error-severity levels reach a maximum of only  $I_i \leq 2$  near such strong vortices. Moderate error-severity levels ( $I_i = 2$ ) at the blunt trailing edge are triggered by the singular points at both corners, where weak oscillations are expected. The flowfield around the trailing edge was examined carefully, but neither the numerical stability of the simulation, nor the main flow phenomena, seem to be significantly affected by those oscillations. Error-severity levels of  $I_i = 2$  are also detected near the leading edge stagnation point and above the supersonic region on the suction side at  $x \approx 0.05$ . The  $z$ -vorticity ( $\omega_z$ ) field in figure 3(B) shows spurious structures that are generated in the farfield due to poorly-resolved upstream-travelling pressure waves. Those weak oscillations (in the order of  $|\omega_z| \approx 0.1$ ) upstream of the airfoil are captured by the error-severity indicator showing error-severity levels of  $I_i = 1$ . After 11 time units, the 6<sup>th</sup>-order filter is engaged and clears up the flowfield significantly. Eventually, the  $\omega_z$ -contour plot in figure 3(C) at  $t = 11.8$  does not exhibit spurious structures as seen in figure 3(B) at an earlier time.

The spectral error-indicator is also applied to the snapshot at  $t = 11.8$  and error-severity levels are plotted in figure 4(A). The error-severity around the leading edge drops below  $I_i = 2$ , whereas increased errors are detected within the transition region and in the vicinity of large vortex structures. The close-ups in figure 4(i/ii) show Q-criterion surfaces ( $Q = 10^4$ ) coloured by vorticity magnitude near the critical regions with  $I_i = 3$  on the suction side (i) and pressure side (ii), where streaky structures break down to turbulence.

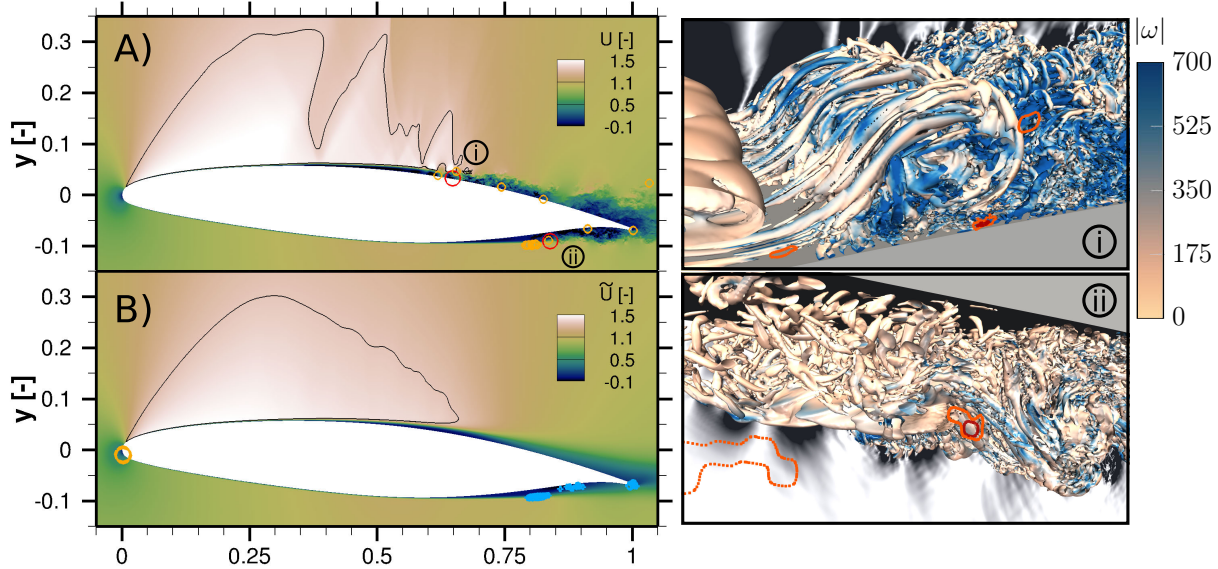


**Figure 4:** (A) Instantaneous snapshot ( $t = 11.8$ ) and (B) time- and span-averaged contours of  $x$ -component of velocity for case  $Nc_{3D}$ . Error-severity levels 1, 2 and 3 are displayed by blue, orange and red circles, respectively. Error-indicator results in (B) are averaged over 2000 snapshots after switching on the filter. The black curves denote the sonic line ( $M = 1$ ). Regions (i) on the suction side and (ii) on the pressure side are magnified and Q-criterion iso-surfaces ( $Q = 10^4$ ) are coloured by vorticity magnitude. Regions of increased error-severity are outlined by correspondingly coloured curves. Except for plot (B), blue circles are not included in order to emphasise the regions of higher error severity in instantaneous snapshots.

The Q-criterion surfaces of small-scale structures seem to be sufficiently resolved and no significant differences are observed in those, compared to adjacent areas with  $I_i \leq 1$ . Considering both instantaneous snapshots, high error-severity is mainly detected in the  $\xi$ -direction close to the transition region, whereas further away from the surface, moderate severity levels ( $I_i = 2$ ) are found in the wall-normal  $\eta$ -direction.

The analysis of instantaneous snapshots gives a good first impression of regions that require attention. As the error-indicator is very sensitive to local features in the flow-field, the results between snapshots vary significantly and therefore, the analysis of single snapshots is not necessarily representative. Therefore, averaged error-severity levels are also calculated, analysing 2000 snapshots ( $\Delta t = 0.004$ ) of case  $Nc_{3D}$  with 6<sup>th</sup>-order filter and plotted on top of the time- and span-averaged  $U$ -velocity field in figure 4(B). Error severity levels of  $0.5 \leq I_i < 1.5$  and  $1.5 \leq I_i < 2.5$  are highlighted by blue and orange circles, respectively. Only the leading edge shows error-severity levels  $I_i \geq 1.5$ , whereas the average error-severity levels drop significantly in the transition regions ( $I_i < 1.5$ ).

### 3.2 Analysis of a 2D simulation

For comparison with the reference 3D case discussed in the previous subsection, results from a 2D simulation were also analysed. Figure 5 shows error-severity levels for a snapshot (A) and an average over 2000 snapshots (B) of a 2D simulation with the

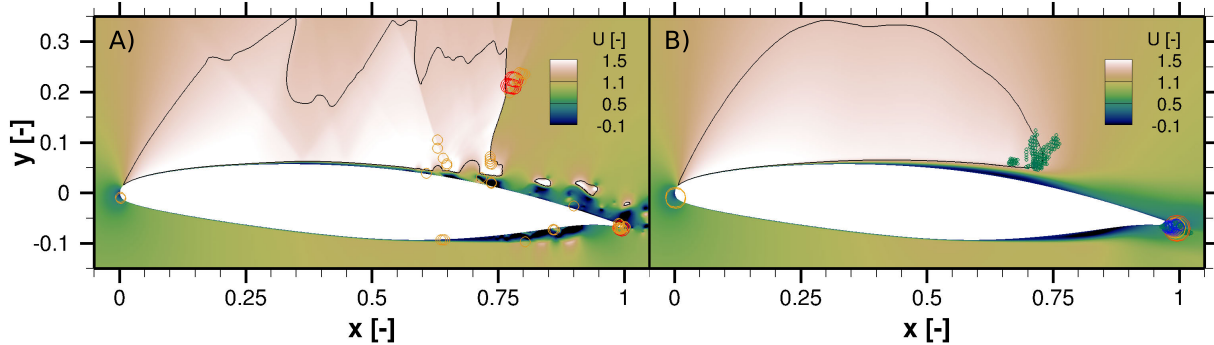


**Figure 5:** (A) Instantaneous snapshot and (B) time- and span-averaged contours of  $u$ -velocity for case  $Nc_{2D}$ . Error-severity levels 0, 1, 2 and 3 are displayed by green, blue, orange and red circles, respectively.

$6^{th}$ -order filter applied for the reference grid  $Nc$ . Low error-severity levels ( $I_i \leq 1$ ) are not shown in figure 5(A). Similar to the error-severity analysis of the 3D simulation, the leading- as well as trailing-edge regions show increased error-severity levels, whereas the trailing edge shows critical values ( $I_i = 3$ ) instead of moderate levels ( $I_i = 2$ ). Moderate error-severity levels are also detected in the vicinity of large vortices. Shock waves can cause instantaneous critical values in the farfield of 2D as well as 3D simulations. The averaged error-severity levels near shear layers are lower for 2D DNS than for the 3D DNS. Error-severity levels of  $I_i \approx 0.2$  (green circles) are observed in figure 5(B) at the end of the supersonic region on the suction-side surface of the airfoil. Even though the 2D simulation is not capable of indicating grid-to-grid point oscillations in the transition region of the 3D simulation, it is even more sensitive to oscillations at the leading- and trailing-edge and can be useful when making initial grid assessments.

### 3.3 Sensitivity analysis

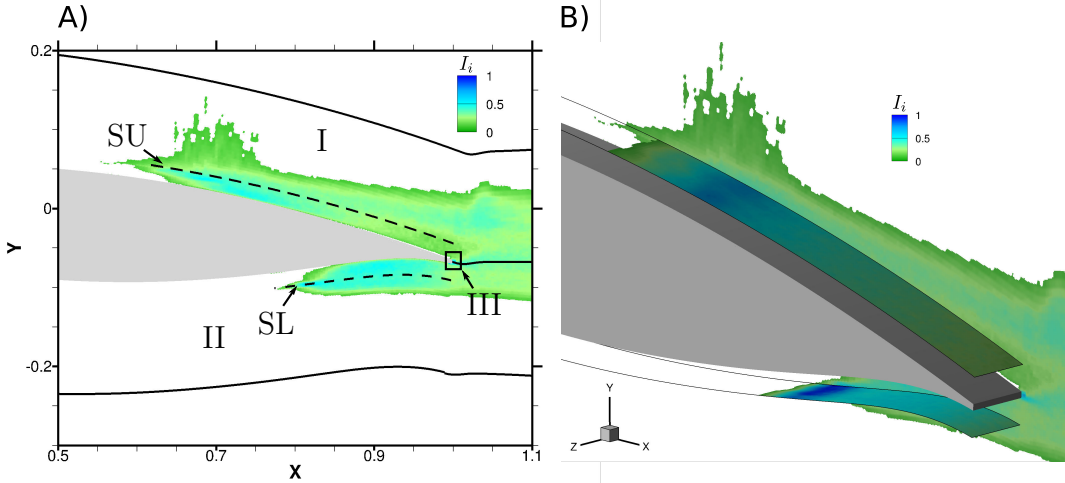
In order to compare results from the error indicator analysis of different cases, the error-indicator results are interpolated onto the reference grid  $Nc$ . An inverse-distance interpolation scheme is applied in Tecplot<sup>TM</sup>, averaging 8 points with a distance exponent of 3.5. Before analysing the refined grids, we need to ensure that there are a sufficient number of points per subdomain ( $N_e^2$ ) for the error-indicator analysis. The error indicator is applied to the instantaneous snapshot in figure 4(A), considering 550 points in the  $\eta$ -direction ( $y|_{\eta=550} - y|_{\eta=1} \approx 1c$ ). The percentage of area corresponding to banded error-severity levels is listed in table 2 for three different settings. The subdomain size of  $N_e = 24$  points results in lower precision and does not capture critical regions with  $I_i \geq 2.5$ . On the other hand, the set up with  $N_e = 12$  points per subdomain is not capable of identifying regions of high error severity, as modes are insufficiently resolved. Therefore, the following grid study will be conducted with the reference setup considering  $N_e = 16$  points per subdomain, as was also suggested by Jacobs et al. (2018).

Figure 6(A) shows the interpolated error-severity levels, neglecting  $I_i \leq 0.1$  and considering an average of 2000 snapshots of the reference case  $Nc_{3D}$  before employing the filter. The area-averaged error-severity levels for  $I_i > 0.1$  are calculated for two sections

Case	$N_e$	$I_i < 0.5$	$0.5 \leq I_i < 1.5$	$1.5 \leq I_i < 2.5$	$2.5 \leq I_i$
$Nc_{3D}^*$	16	99.2 %	0.8 %	$9.6 \cdot 10^{-4}$ %	$3 \cdot 10^{-5}$ %
$Nc_{3D}$	24	99.0 %	1.0 %	$4.2 \cdot 10^{-3}$ %	0 %
$Nc_{3D}$	12	99.2 %	0.8 %	$1.4 \cdot 10^{-3}$ %	0 %

\* reference case

**Table 2:** Fraction of area corresponding to banded error-severity levels for different subdomain sizes.



**Figure 6:** Contour plots showing averaged error-severity levels ( $I_i > 0.1$ ) for case  $Nc_{3D}$ .

( $0.5 < x < 1.1$ ) on the upper surface ( $I$  in figure 6(A)) and lower surface ( $II$  in figure 6(A)), limited in the  $y$ -direction by the solid black curves ( $\eta = 300$ ).

The error indicator is also applied to two  $xz$ -planes going through the shear layers on the upper- and lower-side, labelled as  $SU$  and  $SL$  in figure 6(A), respectively. The area-averaged error-severity levels are calculated, considering only  $I_i > 0.1$ . This tends to underestimate any error-severity reduction, as the improvement due to cells that change from  $I_i > 0.1$  to  $I_i \leq 0.1$  is neglected.

Additionally, the area-averaged error-severity levels are calculated for a rectangle at the trailing edge ( $0.99 < x < 1.01$  and  $-0.0725 < y < 0.06$ ), denoted by  $III$  in figure 6(A), and for a circle around the leading edge (LE) with a radius of 0.055 for  $I_i \geq 0$ . The first line of table 3 lists the resulting averaged values for the reference case  $Nc_{3D}$  considering 2000 snapshots before employing the filter, which is the reference for the sensitivity analysis and grid study. Averaged values are also calculated using 2000 snapshots of case  $Nc_{3D}$  after applying the 6<sup>th</sup>-order filter and a total of 6000 snapshots of the simulation with 2650 snapshots before and 3350 snapshots after switching on the filter. Table 3 summarises the results including deviations from the reference values in brackets. The variation of the average values in the sections  $I - III$  mainly relates to the uncertainty that is caused by the averaging, as the filter should not affect the simulation results in those areas. At

the leading edge, however, the error-severity levels drop dramatically due to the filtering, as already observed in connection with figure 3(C). It was found that analysing only 150 snapshots gives already a very good impression of the range of error-severity levels. The

<i>Case</i>	<i>Filter</i>	#	<i>I</i> ( $\pm\%$ )	<i>II</i> ( $\pm\%$ )	<i>III</i> ( $\pm\%$ )	<i>LE</i> ( $\pm\%$ )
$Nc_{3D}^*$	off	2000	0.251	0.307	0.317	0.091
$Nc_{3D}$	off/on	6000	0.244 (-3%)	0.296 (-4%)	0.319 (8%)	0.040 (-56%)
$Nc_{3D}$	on	2000	0.234 (-7%)	0.293 (-5%)	0.327 (3%)	0.001 (-98%)
$Nc_{3D}^*$	off	150	0.263 (5%)	0.312 (2%)	0.313 (-1%)	0.102 (12%)
$Nc_{2D}$	on	2000	0.194 (-23%)	0.172 (-44%)	0.536 (69%)	0.002 (-98%)

\* reference case

**Table 3:** Values of error-severity levels averaged over different numbers of snapshots (#) and areas (corresponding to figure 6(A)), considering the reference grid  $Nc$ . A circular region around the leading edge with a radius of  $0.05c$  is denoted by  $LE$ .

analysis of region *III*, considering 2D-simulation results, confirms the high sensitivity at the trailing edge, as the average error-severity levels increase by almost 70% compared to the corresponding 3D simulation.

### 3.4 Grid refinement study

For further analysis, only simulation results before employing the filter are considered, averaging the error estimations over 2000 snapshots for each case. For case  $Od_{3D}$ , the reference grid is significantly refined in the  $\eta$ -direction within the shear layer. Furthermore, the grid is refined in the  $\xi$ -direction within the transition region to reduce the error-severity levels near the wall in the vicinity of large vortex structures. The laminar section of the airfoil ( $x < 0.5$ ) is refined as well. An overview of the refined regions is shown in figure 7 comparing the cell size of the grid  $Nc$  and  $Od$ . Dark red regions indicate a significantly increased grid resolution for case  $Od_{3D}$ . As a next step, the reference grid ( $Nc$ ) is only refined in the spanwise direction. For each case, table 4 shows the locally averaged error-severity levels corresponding to the six regions in figure 6. Even though the error-severity of the reference simulation  $Nc_{3D}$  is already low, the  $xy$ -refined grid shows between 25 – 45% lower error-severity levels in the  $xy$ -plane. The error-severity levels in  $xz$ -planes hardly change. The opposite trend is observed for the refinement in the spanwise direction.

## 4 Conclusion and best-practice procedure

A grid generator was developed for smooth multi-block structured grids with blunt trailing edges. Direct numerical simulations were carried out at transonic flow conditions and moderate Reynolds numbers up to half a million. Different grids were tested and analysed with a spectral error-severity indicator. Decreases of averaged error-severity levels are observed in refined regions.

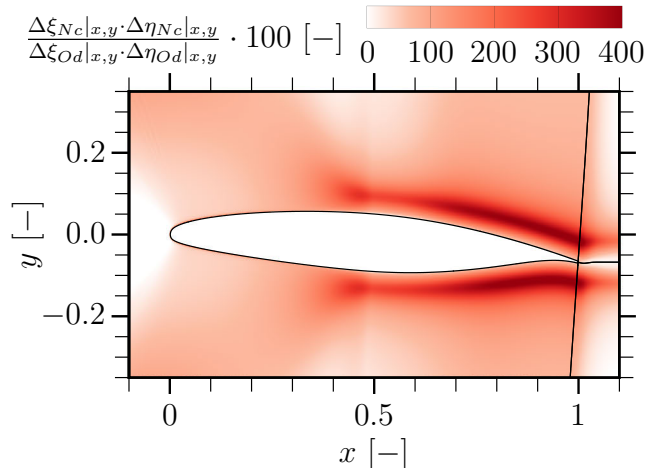


**Figure 7:** Contour plot of the ratio between local cell area values of the grid before and after the refinement.

<i>Case</i>	<i>I</i> ( $\pm\%$ )	<i>II</i> ( $\pm\%$ )	<i>III</i> ( $\pm\%$ )	<i>SU</i> ( $\pm\%$ )	<i>SL</i> ( $\pm\%$ )	<i>LE</i> ( $\pm\%$ )
$Nc_{3D}^*$	0.25	0.31	0.32	0.42	0.52	0.091
$Od_{3D}$	0.18 (-30%)	0.20 (-34%)	0.18 (-45%)	0.48 (-4%)	0.48 (-9%)	0.067 (-26%)
$Nc_{s,3D}$	0.25 (-1%)	0.29 (-6%)	0.31 (-3%)	0.27 (-47%)	0.74 (-48%)	0.093 (-2%)

\* reference case

**Table 4:** Values of error-severity levels averaged over different numbers of snapshots (#) and areas (figure 6(A)) for the grid-study cases.

The error indicator analysis of 2D simulation results captures and even overestimates critical regions at the leading and trailing edge. The leading edge is critical for the generation of an efficient grid, as the minimum Courant number is expected upstream of the stagnation point and limits the time step. Therefore, the error indicator is a useful tool for early stages in the grid-generation process, which can efficiently use 2D simulations. The trailing edge needs to be sufficiently resolved to avoid numerical instabilities near the singular points.

A best-practice procedure was set up with a workflow consisting of the following four steps:

1. Generation and iterative optimisation of the 2D grid. The error-indicator analysis helps to optimise the leading and trailing edge region.
2. Run 3D simulations and analyse instantaneous representative  $xy$ - and  $xz$ -planes to identify critical regions.
3. Calculate averaged error-severity levels for a sufficient number of snapshots to confirm the criticality of identified regions. In the presented case, averages over 150 snapshots were sufficient.

4. Refine the grid in critical regions and repeat the process.

There is also great potential to semi-automate the workflow by including an on-the-fly analysis of simulation results into the next-generation DNS code OpenSBLI (Jacobs et al., 2017).

## 5 Acknowledgement

MZ was supported by EPSRC (award reference 1665277) and the ARCHER Leadership grant, entitled “Transonic flow over an aerofoil” (e509). CTJ was supported by a European Commission Horizon 2020 project entitled “ExaFLOW: Enabling Exascale Fluid Dynamics Simulations” (reference 671571). We would also like to acknowledge Iridis for provided computational resources.

## References

- Carpenter, M. H., Nordström, J., and Gottlieb, D. (1999). A Stable and Conservative Interface Treatment of Arbitrary Spatial Accuracy. *Journal of Computational Physics*, 148(2):341–365.
- Jacobs, C. T., Jammy, S. P., and Sandham, N. D. (2017). OpenSBLI: A framework for the automated derivation and parallel execution of finite difference solvers on a range of computer architectures. *Journal of Computational Science*, 18:12–23.
- Jacobs, C. T., Zauner, M., De Tullio, N., Jammy, S. P., Lusher, D. J., and Sandham, N. D. (2018). An error indicator for finite difference methods using spectral techniques with application to aerofoil simulation. *Computers & Fluids*.
- Sandberg, R. D. and Sandham, N. D. (2006). Nonreflecting Zonal Characteristic Boundary Condition for Direct Numerical Simulation of Aerodynamic Sound. *AIAA Journal*, 44(2):402–405.
- Sandhu, H. and Sandham, N. (1994). Boundary conditions for spatially growing compressible shear layers. Technical report, Faculty of Engineering, Queen Mary and Westfield College, University of London.
- Yao, Y., Shang, Z., and Castagna, J. (2009). Re-Engineering a DNS Code for High-Performance Computation of Turbulent Flows. In *47th AIAA Aerospace Sciences Meeting including The New Horizons Forum and Aerospace Exposition*, Reston, Virginia. American Institute of Aeronautics and Astronautics.
- Zauner, M., De Tullio, N., and Sandham, N. D. (2018). Direct numerical simulations of transonic flow around an airfoil at moderate Reynolds numbers. *Submitted to the AIAA Journal*.
- Zauner, M. and Sandham, N. D. (2018). Multiblock structured grids for direct numerical simulations of transonic wing sections. In *Proceedings of the Tenth International Conference on Computational Fluid Dynamics*, Barcelona.